Why Inverted Small Molecule Solar Cells Outperform Their Noninverted Counterparts

Diana Nanova, Michael Scherer, Felix Schell, Johannes Zimmermann, Tobias Glaser, Anne Katrin Kast, Christian Krekeler, Annemarie Pucci, Wolfgang Kowalsky, Rasmus R. Schröder, and Robert Lovrinčić**

It is shown that the effect of substrate heating on the photo conversion efficiency in vacuum-deposited small molecule organic solar cells is closely related to the improved free charge generation in ordered C_{60} regions. The formation of these ordered regions strongly depends on the deposition sequence in the device and differs therefore between inverted and noninverted cells. Substrate-induced local fullerene ordering is found in small molecule:C_{60} bulk heterojunctions (BHJs) deposited on pristine C_{60} at elevated temperatures. This does not occur for BHJs deposited under identical conditions on pristine donor molecule layers, despite similar degrees of phase separation in both cases. These findings point to a hitherto unidentified advantage of inverted over noninverted solar cells that manifests itself in a higher charge separation efficiency.

1. Introduction

Organic photovoltaics (OPV) remain a highly active field of research despite the recent surge of solar cells based on organometallic perovskite absorbers.[1] The development of power conversion efficiencies (PCE) for vacuum-deposited small molecule organic solar cells has seen an increase from 1% for early two-layer planar devices[2] to certified 12%[3] for cells employing a nondisclosed multibulk heterojunction (BHJ) and 8.3%[4] for single junction cells, respectively. This impressive gain has been spurred by improvements in device architecture,[5] processing,[6] materials,[7] and theoretical understanding.[8] The role of substrate heating during[9] or post[6] BHJ deposition and its impact on PCE via changing the morphology have been studied extensively from early on, however, with mixed results, leading to a clear improvement,[10,11] no change, or even a decrease[12,13] of PCE. Possible morphological effects of temperature treatments on BHJs can be roughly divided into three aspects: relative next neighbor orientation of donor/acceptor molecules,[14,15] mid-range phase separation,[16] and ordering in pure phase-separated regions.[17] The crucial role of delocalized states in ordered fullerene regions for charge separation has been recognized only very recently.[18–21] To the best of our knowledge, a possible influence of device architecture (e.g., the underlying layer) on BHJ morphology and crystallization of individual BHJ components has so far not been considered in literature.

Here, we show that the effect of substrate heating on PCE in vacuum-deposited small molecule organic solar cells is closely related to the formation of ordered C_{60} regions within the BHJ. The C_{60} crystallinity strongly depends on device architecture, namely if the BHJ is evaporated on a pristine C_{60} layer, as in an inverted architecture, or on a pristine absorber layer as in a noninverted architecture. Based on our findings from transmission electron microscopy (TEM), device characterization, and IR spectroscopy studies on the exemplary donor/acceptor system F_4ZnPc/C_{60} (see **Figure 1**a) and a comparison with literature data,[22] we can state that i) for noninverted solar cells heating during deposition has a strong effect on phase separation in the BHJ but not on PCE, whereas ii) in inverted cells heating has a strong effect on phase separation and PCE via a substrate-induced local fullerene ordering and hence improved free charge generation. Our findings elucidate why record efficiencies for vacuum-deposited cells are typically achieved in inverted architecture and have important implications for future development.

Dr. D. Nanova, M. Scherer, Dr. C. Krekeler, Prof. W. Kowalsky, Dr. R. Lovrinčić
Institute for High-Frequency Technology
TU Braunschweig
38106 Braunschweig, Germany
E-mail: r.lovrincic@tu-braunschweig.de

Dr. D. Nanova, M. Scherer, F. Schell, J. Zimmermann, Dr. T. Glaser, A. K. Kast, Dr. C. Krekeler, Prof. A. Pucci, Prof. W. Kowalsky, Prof. R. R. Schröder, Dr. R. Lovrinčić
InnovationLab GmbH
Speyerer Str. 4, 69115 Heidelberg, Germany
E-mail: rasmus.schroeder@bioquant.uni-heidelberg.de

Dr. D. Nanova, F. Schell, J. Zimmermann, Dr. T. Glaser, Prof. A. Pucci, Prof. W. Kowalsky
Kirchhoff Institute for Physics
Heidelberg University
69120 Heidelberg, Germany

A. K. Kast, Prof. R. R. Schröder
Cryo-EM, CellNetworks, BioQuant
Universitätsklinikum Heidelberg
69120 Heidelberg, Germany

A. K. Kast, Prof. A. Pucci, Prof. R. R. Schröder
Centre for Advanced Materials
Heidelberg University
69120 Heidelberg, Germany

DOI: 10.1002/adfm.201502943

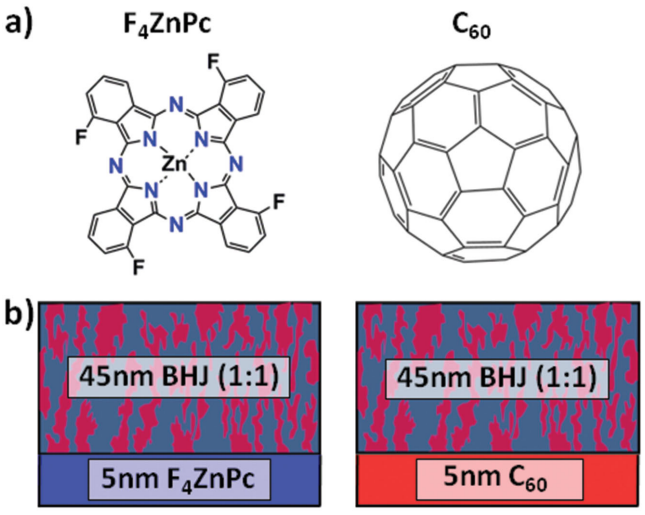

Figure 1. a) Chemical structure of the absorber material F_4ZnPc and the acceptor C_{60}. b) Samples used for the TEM measurements: a BHJ deposited on 5 nm pristine F_4ZnPc, mimicking the noninverted device, and a BHJ deposited on 5 nm pristine C_{60} as used in inverted devices.

2. Energy-Filtered TEM Measurements

To mimic the different growth conditions in noninverted and inverted devices, we deposited BHJ layers for TEM investigations on top of 5 nm of pure F_4ZnPc (as used in noninverted devices) and C_{60} (for inverted devices), respectively (see Figure 1b).

In **Figure 2**, zero-loss (ZL) and energy-filtered images (EFTEM) (18 and 27 eV) are shown for a BHJ (45 nm thickness, volume ratio 1:1) deposited on a pristine F_4ZnPc layer at a) room temperature (RT) and b) 100 °C. The energy-filtered images at 18 and 27 eV are shown representative as they exhibit the strongest contrast inversion due to the energy loss spectral features of F_4ZnPc and C_{60} (see the Supporting Information). At 18 eV and 27 eV energy loss, F_4ZnPc-rich domains and C_{60}-rich domains are expected to appear bright, respectively. The ZL and EFTEM images of the BHJ deposited at RT (Figure 2a) do not show any characteristic features. Accordingly, as no phase separation of F_4ZnPc and C_{60} is noted, the blend deposited at room temperature seems to be homogeneously intermixed. This result is in agreement with published TEM measurements on related material systems, which do not indicate phase separation when deposited at room temperature, e.g., ZnPc:C_{60} blends,[23] as well as cross-sections of CuPc:C_{60} blends deposited on pristine CuPc.[24]

However, the ZL images change dramatically when the BHJ is deposited on F_4ZnPc at an elevated substrate temperature (Figure 2b). The blend exhibits pronounced round, dark structures already in the ZL image. Two characteristic features are marked with red circles. The same features appear dark in the 18 eV and bright in the 27 eV EFTEM image. A more detailed analysis of an entire EFTEM image stack (see the Supporting Information) revealed that these features are C_{60} agglomerates, which are surrounded by F_4ZnPc-rich domains. Hence, the

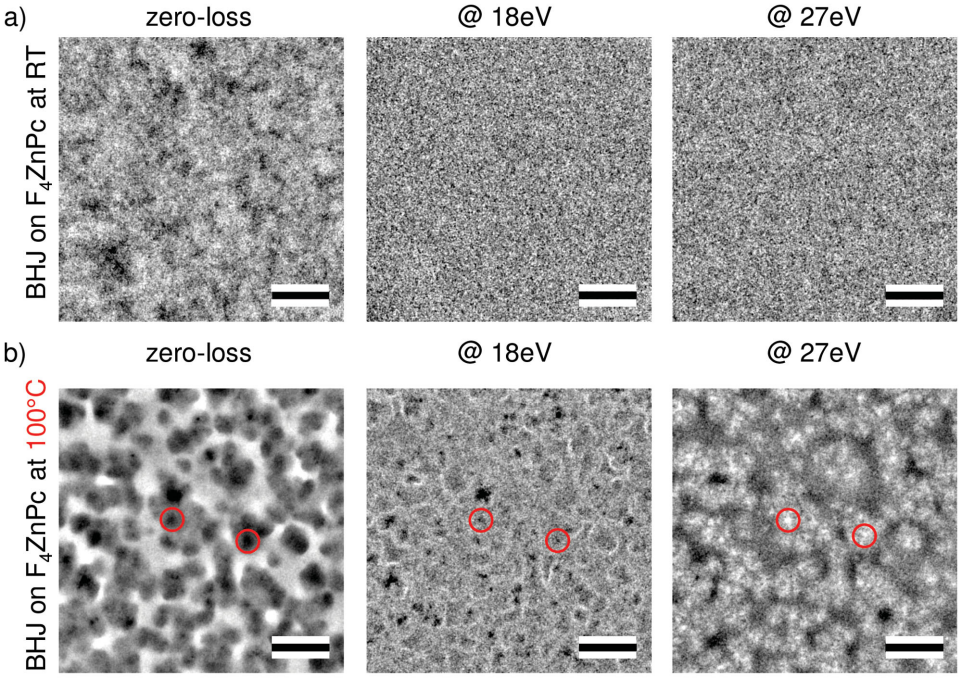

Figure 2. Zero-loss and energy-filtered images of BHJs on 5 nm pristine F_4ZnPc (mimicking the noninverted device) deposited at a) RT and b) 100 °C. The RT sample appears homogenously mixed. The heated sample exhibits pronounced agglomerates (exemplarily marked with red circles), which show a contrast inversion in the energy-filtered images. The agglomerates appear bright at 27 eV energy loss, which is characteristic for C_{60}. All scale bars correspond to 100 nm.

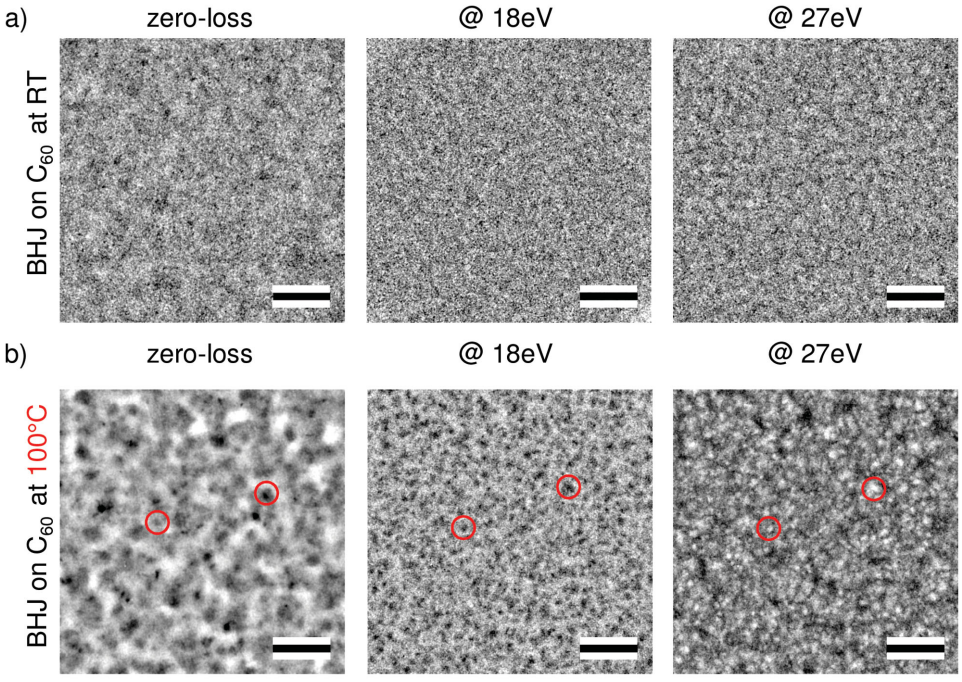

Figure 3. Zero-loss images of BHJs on 5 nm pristine C_{60} (mimicking the inverted device) deposited at a) RT and b) 100 °C. The RT sample appears to be similar to the BHJ on F_4ZnPc, showing no characteristic features. The heated sample exhibits pronounced agglomerates (exemplarily marked with red circles), which show a contrast inversion in the energy-filtered images. The agglomerates appear bright at 27 eV energy loss, which is characteristic for C_{60}. All scale bars correspond to 100 nm.

heating of the substrate during the blend deposition induces a strong phase separation between the donor and acceptor.

In analogy, **Figure 3** shows ZL and EFTEM images of a BHJ deposited on a pristine C_{60} layer, as it is employed in inverted solar cells, at a) RT and b) at 100 °C. The textures of the images for the RT sample (Figure 3a) appear homogenous, indicating predominant mixing rather than segregation. The blend deposited on a heated C_{60} substrate (Figure 3b) exhibits, similar to the blend from Figure 2b, dark agglomerates that change their contrast in the EFTEM images and appear bright at 27 eV energy loss. Two characteristic features are marked with red circles. Accordingly, the dark features in the ZL image are attributed to C_{60} agglomerates. The typical size of the agglomerates is smaller than in the BHJ deposited on heated F_4ZnPc.

In order to investigate the nature of these features appearing for blends deposited at 100 °C in detail, a whole EFTEM image stack from 2 to 35 eV in 1 eV steps was acquired and evaluated with multivariate statistical analysis[16] and plasmon peak mapping.[23] As both methods yielded very similar findings, only the results of the more intuitive plasmon peak mapping are shown in **Figure 4** (see the Supporting Information for results from multivariate statistical analysis). An Otsu threshold[25] is applied so that the difference between the plasmon peaks of both materials is maximal, resulting in a two-class segmentation for the blend a) on a F_4ZnPc support or b) on a C_{60} support. F_4ZnPc-rich domains are indicated in blue and C_{60} agglomerates are indicated in red. The difference in the typical structure size, already visible in the ZL images, is now even more apparent. For the estimation of size distribution and mean distance of the domains, power spectral density analysis was applied (see the Supporting Information). The blend deposited on F_4ZnPc exhibits mainly features between 30 and 70 nm. For the sample on C_{60}, mainly domains and distances between the domains of up to 30 nm are determined, however, with a significant amount of features between 3 and 5 nm. Additionally, the area ratios of F_4ZnPc and C_{60} from the classification are calculated for both samples: 25.4% (C_{60}) and 74.5% (F_4ZnPc) for the sample on F_4ZnPc and 30.5% (C_{60}) and 69.5% (F_4ZnPc) for the sample on C_{60}. It is striking that in both cases the amount of C_{60} areas is significantly lower than could be expected for coevaporated blends in a 1:1 ratio. Hence, we conclude that the assigned F_4ZnPc rich domains still hold a significant amount of intermixed C_{60}.

In conclusion, the TEM measurements clearly show that phase separation between F_4ZnPc and C_{60} occurs when the

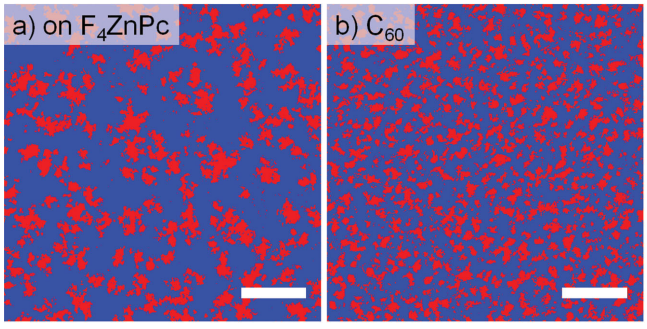

Figure 4. Two class segmentation from plasmon peak mapping of F_4ZnPc (blue) and C_{60} (red) of BHJs deposited at $T = 100$ °C on a) F_4ZnPc (noninverted) and b) C_{60} (inverted). All scale bars correspond to 100 nm.

substrate is heated during the BHJ deposition. The segregation is independent on the substrate and is present on both a pristine F_4ZnPc and a pristine C_{60} layer. In the following, the influence of the morphological changes upon substrate heating on the device performance is investigated.

3. Device Characteristics of Noninverted Solar Cells

Figure 5 shows current–voltage curves for two F_4ZnPc/C_{60} noninverted BHJ solar cells fabricated under identical conditions with the only difference that the substrate was held at 100 °C or RT during coevaporation of the active layer deposition. The inset depicts the used noninverted device layer stack (indium tin oxide (ITO)/MoO_3/F_4ZnPc/F_4ZnPc:C_{60} 1:1/C_{60}/2,2′,2″-(1,3,5-benzinetriyl)-tris(1-phenyl-1-*H*-benzimidazole) (TPBi)/Ag). The two curves almost coincide with no significant difference in open circuit voltage (V_{oc}), short current density (J_{sc}), or fill factor (*FF*). We note that a PCE of around 3% is in the range of best values for noninverted cells based on phtalocyanine absorbers.[6,9,26] The equal performance of the devices is surprising given the completely distinct morphology of the active layer determined from the TEM measurements (see Figure 2). In contrast, Meiss et al.[22] showed that substrate heating to 100 °C during BHJ deposition leads to a clear improvement of PCE by almost 30% for inverted cells with the same BHJ composition (3.6% for the RT and 4.6% for the heated device). We note that the higher total efficiencies reported by Meiss et al. are partially due to the doped transport layers employed in their inverted devices. However, the relative changes upon heating should correlate solely to changes within the BHJ layers, as for both types of cells heating was applied only during the BHJ codeposition. We therefore use Meiss et al.'s results as reference for the inverted device data throughout this work. Reproducing their device efficiency results would be technically very challenging due to a limited availability of the transport layer dopants and is beyond the scope of this work.

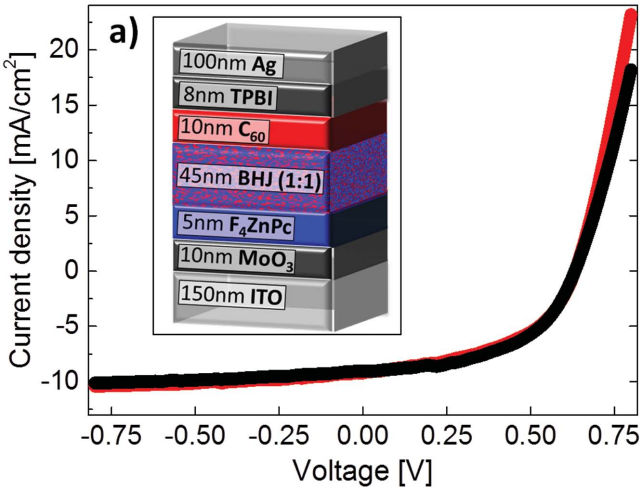

Figure 5. *I–V* characteristics of the best cells (noninverted) deposited on substrates at $T = 100$ °C (red) and $T =$ RT (black). The two cells show very similar performances. The inset depicts the used device stack.

Table 1. The effect of substrate heating on PCE for noninverted (values averaged for eight samples each) solar cells.

	T_{Sub}	V_{oc} [mV]	J_{sc} [mA cm^{-2}]	*FF* [%]	η [%]
Noninverted	RT	628 ± 9	9.1 ± 0.1	50.2 ± 2.2	2.9 ± 0.1
	100 °C	636 ± 9	9.0 ± 0.1	48.1 ± 0.6	2.8 ± 0.1

Table 1 summarizes our noninverted device characteristics for cells fabricated at RT and 100 °C. The improved PCE for cells deposited at 100 °C in inverted structure can be attributed to increases in FF and J_{sc}. Based on surface morphology characterizations, Meiss et al. assigned this effect to a more favorable BHJ morphology, which is in agreement with the observed phase separation in our TEM measurements (Figure 3). The heating-induced segregation of the donor and acceptor leads to a well formed network and healed charge carrier percolation paths, which therefore results in a more efficient charge generation and a higher short circuit current. However, why does substrate heating not have an impact on the PCE of noninverted devices although the active layer also exhibits phase separation upon substrate heating? In order to elucidate these observations we performed electron diffraction measurements on the same samples as used for the EFTEM images.

4. Electron Diffraction

In **Figure 6**a, diffraction patterns of BHJs on F_4ZnPc (top) and on C_{60} (bottom) deposited at 100 °C are shown. The patterns for both samples exhibit three distinct rings. For the BHJ on F_4ZnPc speckles (black distinct spots) within the middle ring become visible, indicating the presence of larger crystalline domains compared to the pattern of the BHJ on F_4ZnPc at RT (see the Supporting Information). The amount of speckles in the pattern of the blend on C_{60} is significantly higher than for the blend on F_4ZnPc, implying a higher degree of crystallinity. Furthermore, in the diffraction pattern of the blend on C_{60} a double ring is visible in the middle feature. This also indicates an increased order in the BHJ when deposited on a heated C_{60} substrate.

For a more detailed comparison, the radial profiles of samples deposited at RT (top) and at 100 °C (bottom) are shown in Figure 6b. The profiles of pristine F_4ZnPc and C_{60} are shown with broken lines in blue and green, respectively. The RT sample on F_4ZnPc (black) exhibits only three broad peaks revealing a rather amorphous nature of the blend. The shoulder at a spacing of 1.34 nm (q = 0.75 nm^{-1}) can be assigned to the (010) peak of F_4ZnPc. The C_{60} (111) peak (0.85 nm, q = 1.18 nm^{-1}) is significantly broadened and slightly shifted. Instead of the next two peaks for pristine C_{60} one broad peak at 0.48 nm is found in the BHJ, which is in good agreement with a peak at 0.46 nm (2.17 nm^{-1}) measured for ZnPc:C_{60} blends.[27] The peak in the profile at 0.34 nm (2.94 nm^{-1}) is again associated with F_4ZnPc and strongly broadened. The radial profile of the sample at room temperature on C_{60} (top, red dashed) resembles the radial profile of the room temperature sample on F_4ZnPc. This indicates that the RT films on both substrates exhibit only short range order and that the sub-

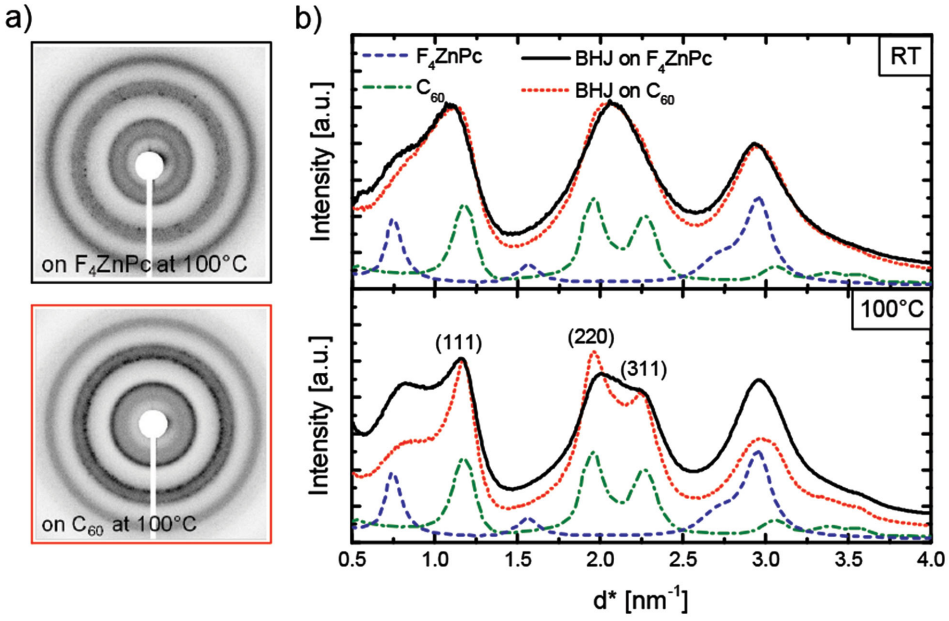

Figure 6. Radial profiles of diffraction patterns of 45 nm thick BHJs on 5 nm of F_4ZnPc and C_{60} deposited at RT (top) and 100 °C (bottom). The dashed lines indicate the profiles of pure F_4ZnPc and C_{60} layers deposited at RT. The profiles of the BHJs at RT are very similar in both cases. The crystallinity of the BHJ on C_{60} at 100 °C increases significantly; the (111), (220), and (311) peaks of C_{60} appear clearly.

strate does not have a significant effect on the crystallization in the BHJ under these conditions. In the radial profile of the heated blend on F_4ZnPc (bottom, black), the peaks associated with F_4ZnPc are slightly more pronounced, but still broadened. The same applies to the C_{60} peaks.

A more significant temperature-induced change is observed in the radial profile of the BHJ deposited on C_{60} (bottom, red dashed). All peaks assigned to C_{60} are very pronounced in the blend. Whereas the F_4ZnPc shoulder in the first peak increases only slightly, the feature at 0.85 nm is strongly enhanced, well separated, and in perfect agreement with the (111) peak in pure C_{60}. Additionally, the two peaks for the pristine material at 0.51 nm (1.96 nm^{-1}, (220)) and 0.44 nm (2.27 nm^{-1}, (311)) along with the small features at $q = 3.5$ nm^{-1} are clearly noticeable.

It can be excluded that the features of crystalline C_{60} in the blend arise from the C_{60} substrate as otherwise they should have also been visible in the RT sample deposited on the same underlayer, which is not the case. Further, it is ruled out that postannealing of the C_{60} underlayer could cause such features, as the radial profile of the pristine material does not exhibit any changes after heating (see Figure S6 in the Supporting Information). Thus, the peaks in Figure 6a in the BHJ on C_{60} are attributed to the strong crystallization of C_{60} within the blend. We conclude that the C_{60} underlayer offers crystallization seeds for the afterward coevaporated C_{60} in the blend. However, the seeds offered by the substrate are not enough to trigger the crystallization process at RT as crystalline C_{60} is not observed in the RT sample on C_{60}. Obviously, the crystallization process is provoked only if accompanied by additional activation energy from the heated substrate. The elevated temperature promotes diffusion of the molecules. Hence, the crystallization seeds provided by the substrate in combination with the higher molecular diffusion lengths cause the crystallization of C_{60} in the blend. Taking the demonstrated phase separation from the previous section into account, we conclude that the found agglomerates mainly consist of crystalline, highly pure C_{60}.

5. IR Spectroscopy

As the electron diffraction results are ambiguous regarding the impact of temperature and underlayer on the F_4ZnPc ordering, we performed IR spectroscopy measurements to further elucidate a possible role of the F_4ZnPc orientation on the device performance. At normal incidence of IR light, only molecular vibrations with a vibrational dipole moment parallel to the substrate can be excited. From this condition follows for the almost planar molecule F_4ZnPc that the intensity of in-plane (ip) modes decreases and the intensity of out-of-plane (oop) modes increases, the more upright the molecules are standing on the substrate. Hence, the intensity ratio of the oop and ip modes is a measure for the average orientation of the molecules in the layer. In **Figure 7**, the IR spectra of a pure layer of F_4ZnPc deposited on Si at RT and the BHJs deposited on F_4ZnPc and C_{60} at 100 °C are shown. From a comparison with a density functional theory (DFT)-calculated spectrum (see Figure S8 in the Supporting Information), the two strongest absorption bands in the selected frequency range can be assigned to an oop vibration and an ip mode, respectively, of F_4ZnPc. The intensity ratio of the oop to ip mode in both BHJ spectra is identical. This shows that the average orientation of the F_4ZnPc molecules in the BHJ deposited at elevated temperature does not depend on the underlying layer. Based on these results, we exclude a change of relative donor–acceptor orientation[14,15] in the BHJ as main cause for the improved PCE in inverted cells deposited at elevated temperatures.

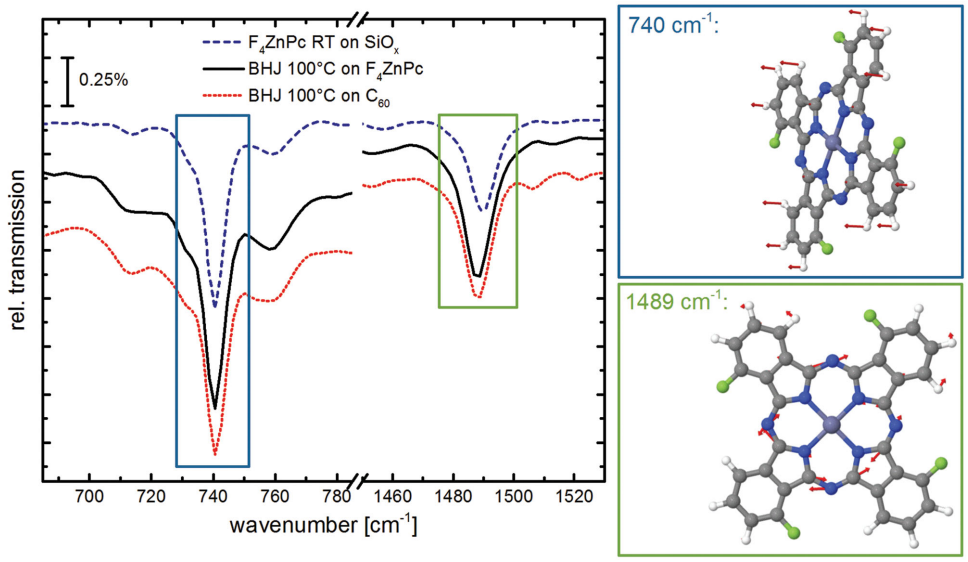

Figure 7. Relative transmittance at normal incidence (for a selected spectral range and the bare substrate as reference) of 14 nm F_4ZnPc on SiO_x and BHJs on C_{60} and on F_4ZnPc at 100 °C (left panel). The red arrows in the molecular structure (right panels) indicate the atomic displacement vectors of the out-of-plane C–H deformation vibration at 740 cm^{-1} and the in-plane C–N stretching vibration at 1489 cm^{-1}. There is no significant change in the ip/oop mode ratio between the two BHJs, indicating no or only little change in F_4ZnPc orientation.

6. Conclusions

We started with the surprising finding that substrate heating does not improve the PCE for noninverted solar cells, although TEM investigations revealed that heating induces a strong phase separation in the active layer. We found two main differences for the BHJs grown on C_{60} and F_4ZnPc mimicking the situations in noninverted and inverted cell architectures. First, the typical domain size for phase separated regions is larger on F_4ZnPc than on C_{60}. On F_4ZnPc, the driving force for phase separation is a thermally activated dewetting of C_{60} induced by the lower surface energy for the phtalocyanine.[28] On C_{60}, the high C_{60}–C_{60} diffusion barrier[29] leads to smaller agglomerates. The larger average domain size (30–50 nm) and distance between domains might be partially responsible for the lack of PCE improvement in the noninverted cell, as it is in the range of the exciton diffusion length in C_{60} (≈40 nm[30]).

The second, and in our perspective more important difference for the BHJs grown at elevated temperatures, is the local C_{60} ordering which improves only for the BHJ grown on C_{60} at elevated temperatures, as revealed by electron diffraction. It is now well established that enhanced charge carrier delocalization accompanied by higher electron mobilities in crystalline fullerene domains leads to a more efficient charge separation, which triggers exciton dissociation directly into free electrons and holes.[18,19] Due to the independence of exciton dissociation on applied voltage, the fill factor of solar cells with crystalline C_{60} domains is expected to increase.[31] Such an increase in FF was indeed observed for inverted devices where the blend is deposited on a pristine C_{60} layer,[11,22,32] whereas in this work and several others[12,13,23] no improvement for noninverted devices was achieved. We conclude that substrate heating is a necessary but not sufficient prerequisite for an optimal BHJ composition. Only if combined with a substrate-induced local fullerene ordering—as it is found in inverted devices—does the increased molecular diffusion at elevated temperature significantly improve PCE.

We note that TEM measurements represent the projection of the entire bulk, hence the exact 3D position of crystallites and domains within the film with respect to the surface and substrate is not determined. However, vertical segregation might as well play a crucial role for device performance. A thickness dependent growth of elongated donor and acceptor islands was as well observed for diindenoperylene (DIP):C_{60} blends.[33] If these columnar structures are available for direct percolation paths through the device, anisotropic charge transport might improve the solar cell. Ongoing TEM tomography studies will answer this question.

In summary, we have shown that the effect of substrate heating on the PCE of small molecule solar cells is more subtle than previously believed: higher molecular diffusion at elevated temperature promotes phase separation in the BHJ, but this alone does not necessarily lead to an increase in efficiency. The phase separated areas are still largely amorphous, if the BHJ is grown on the donor material. However, if the BHJ is grown on an underlying C_{60} layer, as it is typically the case for inverted devices, substrate-induced local fullerene ordering occurs. These highly pure and ordered C_{60} domains improve free charge carrier generation and hence device efficiency. Besides clarifying why record efficiencies are achieved in inverted architecture[4] and literature reports on the effect of substrate heating on PCE show mixed results, our findings might point to a new direction in OPV development: if a device architecture and material combination could be found that allow not only the acceptor but also the donor in the BHJ to form highly ordered domains, the disorder related loss in V_{oc} that OPV suffers from in general[34] might be partially overcome.

7. Experimental Section

Materials: MoO_3 (>99.99%) and Ag (>99.9999%) were purchased from Sigma-Aldrich, TPBI was purchased from Sensient Technologies, C_{60} (>99.9%) was purchased from American Die Society, and F_4ZnPc was provided by BASF SE.

Solar Cell Fabrication and Characterization: Patterned indium tin oxide (ITO) substrates were cleaned in an ultrasonic bath with isopropyl alcohol/acetone and oxygen plasma treated afterwards. MoO_3, organic layers, and Ag top contact were deposited via vacuum sublimation at a base pressure of $\leq 10^{-7}$ mbar ($\leq 5 \times 10^{-7}$ mbar while processing organics and $\leq 5 \times 10^{-6}$ mbar while processing metal/MoO_3). Same deposition rates (±20%) were used for all presented samples, in detail: MoO_3: 1.5 nm min^{-1}; F_4ZnPc: 1 nm min^{-1}; C_{60}: 1 nm min^{-1}; TPBI: 1 nm min^{-1}; Ag: 8 nm min^{-1}; and F_4ZnPc:C_{60} coevaporation: [1+1] nm min^{-1}. After their preparation in vacuum, the samples were transferred and characterized under nitrogen atmosphere, ensuring no exposure to ambient before and during characterization. A calibrated solar simulator from LOT-QuantumDesign with 1.5 air mass (AM) solar spectrum was used for IV characterization. The solar cells had an active area of 4 mm^2.

TEM Sample Preparation: All TEM samples were evaporated onto a poly(3,4-ethylenedioxythiophene) (PEDOT):poly(styrenesulfonate) (PSS) (step 1: 4300 rpm, 1000 rpm for 10 s; step 2: 4300 rpm, 4300 rpm for 30 s; annealing for 30 min at 140 °C) coated ITO glass. The films were floated off the substrate in demineralized water in which the PEDOT:PSS dissolves and collected with a copper grid (200 mesh) coated with a holey carbon film QUANTIFOIL (3.5/1).

TEM Measurements: All measurements were performed with a Libra 200 MC KRONOS, Carl Zeiss Microscopy at 60 keV acceleration voltage. The microscope is equipped with a monochromator combined with an in-column energy filter leading to a spectroscopic resolution of about 90 meV. The total electron dose applied for electron energy loss spectroscopy was 10^2 electrons per nm^2, for electron diffraction 10^3 electrons per nm^2, and for electron spectroscopic imaging (ESI) series 10^6 electrons per nm^2. Energy-filtered images (ESI series) from 2 to 35 eV were acquired in steps of 1 with a 2 eV wide slit aperture.

IR Spectroscopy: All measurements were performed in a custom designed ultrahigh vacuum (UHV) chamber with a base pressure below 2×10^{-9} mbar that is connected to a Bruker Vertex80v Fourier-transform IR spectrometer. The IR beam was coupled out of the spectrometer and focused on the sample that is located in the UHV chamber. The transmitted beam was measured with a liquid nitrogen cooled mercury-cadmium-telluride detector that is located outside the UHV chamber. The organic films were deposited onto the Si substrate inside the same UHV chamber and IR spectra were taken directly after film deposition with a resolution of 4 cm^{-1}. For the spectra of the BHJs, directly after deposition of the F_4ZnPc or C_{60} layer, respectively, the substrate was heated to 100 °C before deposition of the BHJ and measurement of the IR spectrum. The spectra of the BHJs are referenced to the spectrum of the F_4ZnPc or C_{60} layer, respectively, on Si (wafer with natural oxide SiO_x) at elevated temperature. The spectrum of the pristine F_4ZnPc layer is referenced to the spectrum of the bare Si substrate. Substrate temperature was controlled with a calibrated thermocouple (type N) that was attached in direct vicinity to the sample holder.

DFT Calculations: Calculated IR spectra have been obtained using DFT with the B3LYP exchange and correlation functional and the def2-SVP basis set. The geometry for the neutral F_4ZnPc was first optimized and then the vibrational spectrum was obtained. For all calculations the TURBOMOLE 6.5 package has been used. The calculated frequencies were scaled with the factor 0.9614.[35]

Supporting Information

Supporting Information is available from the Wiley Online Library or from the author.

Acknowledgements

D.N. and M.S. contributed equally to this work. The authors thank Peter Erk (BASF SE) for providing F_4ZnPc and valuable discussions. The authors acknowledge financial support from the German Ministry of Education and Research (FKZ 13N10794 and 03EK3505K/L/M).

Received: July 16, 2015
Revised: September 3, 2015
Published online: September 30, 2015

[1] P. K. Nayak, D. Cahen, *Adv. Mater.* **2014**, *26*, 1622.
[2] C. W. Tang, *Appl. Phys. Lett.* **1986**, *48*, 183.
[3] T. Ameri, N. Li, C. J. Brabec, *Energy Environ. Sci.* **2013**, *6*, 2390.
[4] R. Meerheim, C. Körner, K. Leo, *Appl. Phys. Lett.* **2014**, *105*, 063306.
[5] M. Hiramoto, H. Fujiwara, M. Yokoyama, *Appl. Phys. Lett.* **1991**, *58*, 1062.
[6] P. Peumans, S. Uchida, S. R. Forrest, *Nature* **2003**, *425*, 158.
[7] K. Schulze, C. Uhrich, R. Schüppel, K. Leo, M. Pfeiffer, E. Brier, E. Reinold, P. Bäuerle, *Adv. Mater.* **2006**, *18*, 2872.
[8] C. Poelking, M. Tietze, C. Elschner, S. Olthof, D. Hertel, B. Baumeier, F. Würthner, K. Meerholz, K. Leo, D. Andrienko, *Nat. Mater.* **2014**, *14*, 434.
[9] K. Suemori, T. Miyata, M. Yokoyama, M. Hiramoto, *Appl. Phys. Lett.* **2005**, *86*, 063509.
[10] C. Schünemann, D. Wynands, L. Wilde, M. P. Hein, S. Pfützner, C. Elschner, K.-J. Eichhorn, K. Leo, M. Riede, *Phys. Rev. B* **2012**, *85*, 245314.
[11] S. Pfuetzner, C. Mickel, J. Jankowski, M. Hein, J. Meiss, C. Schuenemann, C. Elschner, A. A. Levin, B. Rellinghaus, K. Leo, M. Riede, *Org. Electron.* **2011**, *12*, 435.
[12] K. Fostiropoulos, W. Schindler, *Phys. Status Solidi B* **2009**, *246*, 2840.
[13] S. O. Djobo, L. Cattin, M. Morsli, A. Godoy, F. R. Diaz, M. A. del Valle, J. C. Bernède, in *AIP Conf. Proc.* (Eds: P. Predeep, M. Thakur, M. K. Ravi Varma), AIP, New York **2011**, 251.
[14] B. P. Rand, D. Cheyns, K. Vasseur, N. C. Giebink, S. Mothy, Y. Yi, V. Coropceanu, D. Beljonne, J. Cornil, J.-L. Brédas, J. Genoe, *Adv. Funct. Mater.* **2012**, *22*, 2987.
[15] A. Ojala, A. Petersen, A. Fuchs, R. Lovrincic, C. Pölking, J. Trollmann, J. Hwang, C. Lennartz, H. Reichelt, H. W. Höffken, A. Pucci, P. Erk, T. Kirchartz, F. Würthner, *Adv. Funct. Mater.* **2012**, *22*, 86.
[16] M. Pfannmöller, H. Flügge, G. Benner, I. Wacker, C. Sommer, M. Hanselmann, S. Schmale, H. Schmidt, F. A. Hamprecht, T. Rabe, W. Kowalsky, R. R. Schröder, *Nano Lett.* **2011**, *11*, 3099.
[17] L. A. Perez, K. W. Chou, J. A. Love, T. S. van der Poll, D.-M. Smilgies, T.-Q. Nguyen, E. J. Kramer, A. Amassian, G. C. Bazan, *Adv. Mater.* **2013**, *25*, 6380.
[18] B. Bernardo, D. Cheyns, B. Verreet, R. D. Schaller, B. P. Rand, N. C. Giebink, *Nat. Commun.* **2014**, *5*, 3245.
[19] B. M. Savoie, A. Rao, A. A. Bakulin, S. Gelinas, B. Movaghar, R. H. Friend, T. J. Marks, M. A. Ratner, *J. Am. Chem. Soc.* **2014**, *136*, 2876.
[20] S. Gélinas, A. Rao, A. Kumar, S. L. Smith, A. W. Chin, J. Clark, T. S. van der Poll, G. C. Bazan, R. H. Friend, *Science* **2014**, *343*, 512.
[21] A. F. Bartelt, C. Strothkämper, W. Schindler, K. Fostiropoulos, R. Eichberger, *Appl. Phys. Lett.* **2011**, *99*, 143304.
[22] J. Meiss, A. Merten, M. Hein, C. Schuenemann, S. Schäfer, M. Tietze, C. Uhrich, M. Pfeiffer, K. Leo, M. Riede, *Adv. Funct. Mater.* **2012**, *22*, 405.
[23] W. Schindler, M. Wollgarten, K. Fostiropoulos, *Org. Electron.* **2012**, *13*, 1100.
[24] J. B. Gilchrist, T. H. Basey-Fisher, S. C. Chang, F. Scheltens, D. W. McComb, S. Heutz, *Adv. Funct. Mater.* **2014**, *24*, 6473.
[25] N. Otsu, *IEEE Trans. Syst. Man Cybern.* **1979**, *9*, 62.

[26] T.-M. Kim, J. W. Kim, H.-S. Shim, J.-J. Kim, *Appl. Phys. Lett.* **2012**, *101*, 113301.
[27] B. Maennig, J. Drechsel, D. Gebeyehu, P. Simon, F. Kozlowski, A. Werner, F. Li, S. Grundmann, S. Sonntag, M. Koch, K. Leo, M. Pfeiffer, H. Hoppe, D. Meissner, N. S. Sariciftci, I. Riedel, V. Dyakonov, J. Parisi, *Appl. Phys. A* **2004**, *79*, 1.
[28] T. McAfee, E. Gann, H. Ade, D. B. Dougherty, *J. Phys. Chem. C* **2013**, *117*, 26007.
[29] S. Bommel, N. Kleppmann, C. Weber, H. Spranger, P. Schäfer, J. Novak, S. V. Roth, F. Schreiber, S. H. L. Klapp, S. Kowarik, *Nat. Commun.* **2014**, *5*, 5388.
[30] P. Peumans, A. Yakimov, S. R. Forrest, *J. Appl. Phys.* **2003**, *93*, 3693.
[31] P. K. Nayak, K. L. Narasimhan, D. Cahen, *J. Phys. Chem. Lett.* **2013**, *4*, 1707.
[32] S. Pfuetzner, J. Meiss, A. Petrich, M. Riede, K. Leo, *Appl. Phys. Lett.* **2009**, *94*, 253303.
[33] R. Banerjee, J. Novák, C. Frank, C. Lorch, A. Hinderhofer, A. Gerlach, F. Schreiber, *Phys. Rev. Lett.* **2013**, *110*, 185506.
[34] P. K. Nayak, G. Garcia-Belmonte, A. Kahn, J. Bisquert, D. Cahen, *Energy Environ. Sci.* **2012**, *5*, 6022.
[35] A. P. Scott, L. Radom, *J. Phys. Chem.* **1996**, *100*, 16502.